Frontiers of Information Technology & Electronic Engineering
www.jzus.zju.edu.cn; engineering.cae.cn; www.springerlink.com
ISSN 2095-9184 (print); ISSN 2095-9230 (online)
E-mail: jzus@zju.edu.cn

A composite optimization method for separation parameters of large-eccentricity pico-satellites*

Lai TENG†, Zhong-he JIN

School of Aeronautics and Astronautics, Zhejiang University, Hangzhou 310027, China

†E-mail: tenglai@zju.edu.cn

Received June 24, 2017; Revision accepted Aug. 29, 2017; Crosschecked May 4, 2018

Abstract: A spacecraft's separation parameters directly affect its flying trace. If the parameters exceed their limits, it will be difficult to adjust the flying attitude of the spacecraft, and the spacescraft may go off-track or crash. In this paper, we present a composite optimization method, which combines angular velocities with external moments for separation parameters of large-eccentricity pico-satellites. By changing the positions of elastic launch devices, the method effectively controls the popping process under the condition of less change in the separation mechanism. Finally, the reasons for deviation of angular velocities and unreliable optimization results are presented and analyzed. This optimization method is proved through a ground test which offsets the gravity. Simulation and test results show that the optimization method can effectively optimize the separation parameters of large-eccentricity pico-satellites. The proposed method adapts particularly to the fixed and non-stable status elastic parameters, the distribution of all kinds of elastic devices, and large-eccentricity spacecrafts for which attitude corrections are difficult. It is generally applicable and easy to operate in practical applications.

Key words: Pico-satellite; Satellite–rocket separation mechanism; Separation parameters; Parameter optimization
https://doi.org/10.1631/FITEE.1700416 **CLC number:** TH122

1 Introduction

A satellite–rocket separation system ensures a reliable connection between the satellite and rocket. Satellite separation is critical because the dynamic procedure of separation influences the attitude of the satellite. Improper design of a separation system can lead to a poor dynamic procedure, resulting in the failure of launch mission. Therefore, improving the design and analysis methods for separation systems is important for optimization of the dynamic procedure of satellite separation.

The dynamics of satellite separation systems have received considerable attention from many researchers. Somanath et al. (2001) designed a 'ball lock' separation system for microsatellites, and studied the dynamics model and feasibility of reducing shock to learn the release function and to quantify the impact forces. Miyamoto et al. (2005) developed a heat knife-type, non-explosive separation device with a high separation accuracy for the Cubical Tokyo Tech Engineering (CUTE) satellite, called the 'Tokyo Tech pico-satellite orbital deployer (T-POD) separation system'. Lan et al. (2006) designed and developed the poly pico-satellite orbital deployer (P-POD) separation system for standard cubesat satellites; the reliability of the satellite during ascent flight was improved by adopting a closed structure, and the separation accuracy of the satellite was improved by rail-type separation. Wu et al. (2013) designed an open-style satellite–rocket separation system for the ZDPS-2 satellite and proved the feasibility of the system from a theoretical perspective. Hu et al. (2013) conducted analysis on the dynamics and transient perturbation of a piggybacking satellite separation

* Project supported by the National Natural Science Foundation of China (No. 61525403)
ORCID: Lai TENG, http://orcid.org/0000-0003-0329-5302

system, and controlled the minimum relative distance to achieve collision-free separation for the Tiantuo-1 satellite. Wu and Xu (2014) and Xie et al. (2014) designed and analyzed a movement system for the satellite–rocket separation mechanism of the ZDPS-1A satellite, and proved its ability to separate the orbiting satellite and rocket. Paris (2015) developed a four-pin separation system for the LARES satellite, and proved the rationality of the design through vibration tests and on-orbit separation. Note that these studies have focused mainly on microsatellites. In general, engineers need to design special separation systems for microsatellites and analyze their separation properties, because the shapes and separation types of microsatellites are more diverse than those of large satellites.

The clamp band joint is one of the most common satellite separation systems in use currently, especially for large satellites. Numerous studies on the modelling and dynamic analysis of clamp band systems have been performed. Iwasa et al. (2007) proposed a simple model to predict the interface response of a V-band-clamp separation device. With this model, the simplified shock response spectrum curve of the interface corresponding to the pyroshock specification can be determined, and the shock response of the satellite can be predicted. Qin et al. (2009, 2010, 2011, 2012, 2014) carried out a series of studies on the mechanical behavior of the clamp band joint as well as its influence on the dynamic behavior of the launch system during ascent flight through comprehensive applications of the classical elastic theory, dynamic responses of the spacecraft system to vibration and impact excitations, finite element models, and experimental validation. The research results showed that the clamp band joint can achieve its function and be incorporated easily in other types of launch systems. Tan and Yan (2010) analyzed the dynamic properties of satellite separation systems and the influence of component failure; this type of analysis can effectively prevent both collisions between the V-shoes and satellite and the separation attitude deflection of the satellite. Li et al. (2012, 2014) improved the method of Tan and Yan (2010) to design and analyze separation systems, and provided two-dimensional (2D) and three-dimensional (3D) dynamic envelopes of the clamp band, revealing that appropriately increasing the pyroshock and decreasing the stiffness of the restraining spring can guarantee a secure and reliable satellite separation. Cui et al. (2014, 2015) proposed a modeling and simulation method to comprehensively predict the dynamic characteristics of satellite separation, considering the flexibility of the interface rings. The results in Cui et al. (2014, 2015) can aid in developing the initial engineering design of the clamp band joint of a satellite separation system that ensures a secure and reliable separation.

However, these studies focused mainly on the dynamic problems between satellites and satellite separation systems or launch systems. With the ever-increasing importance of highly accurate separation between the satellite and rocket (Huang et al., 2012), it is crucial to study the effects of separation performance (Singaravelu et al., 2011; Huang et al., 2012; Hu et al., 2014a; Chao et al., 2015; Cui et al., 2015) on the separation system, and to analyze and optimize the satellite–rocket separation system dynamics (Jing et al., 2010; Tan and Yan, 2010; Wang et al., 2010; Paris, 2015; Michaels and Gany, 2016). The optimization of satellite separation has received considerable attention from several researchers. Tayefi and Ebrahimi (2009) optimized and practically verified the mass of a separation system using the response surface method; the results showed that this approach not only maintains the desired characteristics of the separation system but also decreases the overall mass considerably. Hu et al. (2013, 2014b) adopted a multi-island genetic algorithm and simplified metric methods to optimize the separation velocity and angular velocities of the Tiantuo-1 satellite, and verified its effectiveness during the on-orbit separation. Hu et al. (2017) established and verified a novel evaluation approach based on active subspace identification and response surface construction; the analysis results showed a considerably high accuracy and efficiency of the approach, demonstrating the wide applicability of this method for improving the separation accuracy of small satellites. Jiang et al. (2015) introduced a method to control the angular velocity of constrained and centroid-biased on-orbit separation, and the moment and angular velocity were controlled effectively and optimized through numerical simulations. Chao et al. (2015) presented a new separation initialization method, which considers the separation parameters including direction, size, and time interval

between two separations while releasing payload satellites. The results showed that this method can provide stable formations for small-satellite cooperation, and longer formations can be formed at higher reference orbits. Teng and Jin (2016) used an orthogonal optimization method to directly optimize the angular velocities of ZDPS-2 and to ensure that they meet separation accuracy requirements. In addition, the optimization results were proved through ground tests and on-orbit separation.

These studies and achievements help researchers understand the importance of dynamic characteristics and the optimization of satellite separation systems. It is essential to introduce an effective method to improve the separation accuracy of the ZDPS satellites. In this paper, we introduce a composite optimization method for large-eccentricity pico-satellites. We redesign the separation system of ZDPS-3 and conduct theoretical analysis, optimization, and tests, to make dynamic characteristics and separation parameters satisfy the technical requirements.

2 Separation dynamics theory

To avoid the sticking caused by redundant constraints during satellite separation, we adopted a locking scheme with six degrees of freedom and non-redundant constraints. Because two supporting rods are arranged at the opposite angles of the satellite, five degrees of freedom are limited. The pre-tightening force of the locking rods, arranged at the opposite angles, clamps the satellite tightly to the separation mechanism. The constrained degrees of freedom formed on the separation mechanism and the relative positions of the locking, supporting, and pushing rods are shown in Figs. 1 and 2, respectively. We installed explosive cutters on the locking rods. During unlocking, the explosive cutters cut the two locking rods simultaneously and the satellite is released by the four pre-compressed springs.

The ZDPS-3A/3B satellites are separated simultaneously in the lateral direction (Fig. 3). The spring forces of the two satellites cancel each other out at the moment of separation, and therefore the rocket remains stationary. Without considering the elastic damping or friction force between the satellite and pushing rods, the velocity equation can be expressed

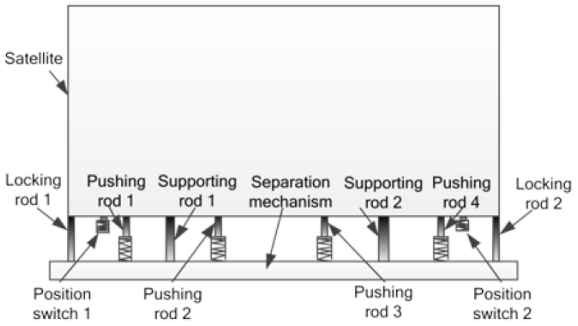

Fig. 1 Freedom constraint on the separation mechanism

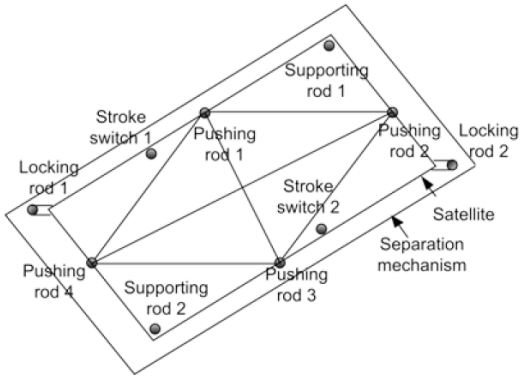

Fig. 2 Relative positions of the locking, supporting, and pushing rods

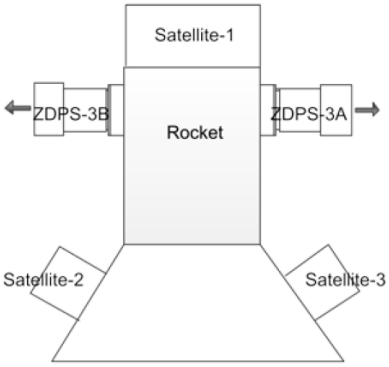

Fig. 3 Installation of the ZDPS-3 satellite on the rocket

according to the principle of conservation of energy:

$$4\left[\frac{1}{2}k(X_0^2-X_1^2)\right]+2\left[\frac{1}{2}k_1(X_2^2-X_3^2)\right]=\frac{1}{2}mV^2, \quad (1)$$

where k is the separation spring stiffness, X_0 the maximum compression of the separation spring, X_1 the minimum compression of the separation spring, k_1 the spring stiffness of the position switch, X_2 the maximum compression of the position switch spring, X_3 the minimum compression of the position switch

spring, m the satellite mass, and V the relative velocity of satellite separation.

The spring force equations can be expressed as

$$F=\begin{cases}-kX\cos(ft), & x_0<X<x_1,\\ -kX, & X=x_1,\end{cases} \tag{2}$$

$$F'=\begin{cases}-k'X'\cos(ft), & x_0<X'<x_1,\\ -k'X', & X'=x_1,\end{cases} \tag{3}$$

where F and F' are the spring forces, k' is the spring stiffness of the position switch spring, X and X' are the spring strokes, x_0 and x_1 are coordinate values, f is the spring frequency, and t is the separation time.

Based on this satellite–rocket separation system, the coordinate system is set up as shown in Fig. 4. The attitude dynamics can be expressed as

$$\begin{cases}I_x\dot{\omega}_x+(I_z-I_y)\omega_y\omega_z=M_x,\\ I_y\dot{\omega}_y+(I_x-I_z)\omega_x\omega_z=M_y,\\ I_z\dot{\omega}_z+(I_y-I_x)\omega_x\omega_y=M_z,\end{cases} \tag{4}$$

where I_x, I_y, and I_z are the principal moments of inertia of the satellite corresponding to the three axes, $\dot{\omega}_x$, $\dot{\omega}_y$, and $\dot{\omega}_z$ are the angular rates of the satellite in the three directions, ω_x, ω_y, and ω_z are the angular velocities of the satellite in the three directions, and M_x, M_y, and M_z are the external moments of the three axes.

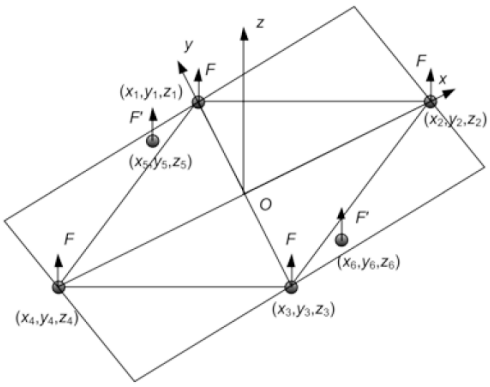

Fig. 4 Original coordinate system

When the mass center of the satellite is at the original point, the external moments can be expressed as

$$\begin{cases}M_x=\sum_{i=1}^{n}F_i\,|\,y_i\,|+\sum_{j=1}^{m}F_j'\,|\,y_j\,|,\\ M_y=\sum_{i=1}^{n}F_i\,|\,x_i\,|+\sum_{j=1}^{m}F_j'\,|\,x_j\,|,\\ M_z=0.\end{cases} \tag{5}$$

When the mass center of the satellite is biased, the coordinate system (Fig. 5) is established. The external moments can be expressed as

$$\begin{cases}M_{x'}'=\sum_{i=1}^{n}F_i\,|\,y_i'\,|+\sum_{j=1}^{m}F_j'\,|\,y_j'\,|,\\ M_{y'}'=\sum_{i=1}^{n}F_i\,|\,x_i'\,|+\sum_{j=1}^{m}F_j'\,|\,x_j'\,|,\\ M_{z'}'=0,\end{cases} \tag{6}$$

$$y'=y-y_{\mathrm{c}}, \tag{7}$$

$$x'=x-x_{\mathrm{c}}, \tag{8}$$

where $(x_{\mathrm{c}}, y_{\mathrm{c}})$ refers to the position of the mass center.

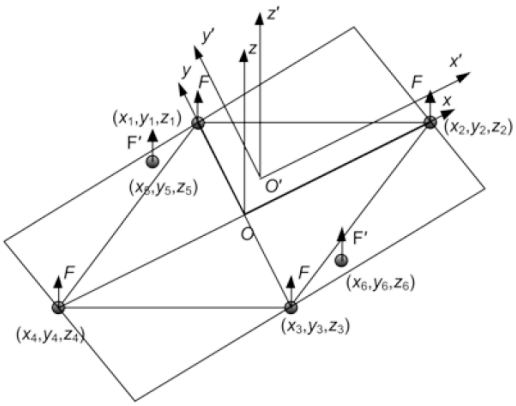

Fig. 5 Biased coordinate system

From Eqs. (6)–(8), it can be seen that the external moments are determined by the mass center of the satellite, the positions of the pushing rods, and the position switches.

In this separation system, when $x_5<x_{\mathrm{c}}$, $x_6>x_{\mathrm{c}}$, $y_5>y_{\mathrm{c}}$, and $y_6<y_{\mathrm{c}}$, the equations of external moments can be expressed as

$$\begin{aligned}M_{x'}=&F\,|\,y_1-y_{\mathrm{c}}\,|-F\,|\,y_2-y_{\mathrm{c}}\,|-F\,|\,y_3-y_{\mathrm{c}}\,|\\ &-F\,|\,y_4-y_{\mathrm{c}}\,|+F'\,|\,y_5-y_{\mathrm{c}}\,|-F'\,|\,y_6-y_{\mathrm{c}}\,|,\end{aligned} \tag{9}$$

$$\begin{aligned}M_{y'}=&F\,|\,x_1-x_{\mathrm{c}}\,|-F\,|\,x_2-x_{\mathrm{c}}\,|+F\,|\,x_3-x_{\mathrm{c}}\,|\\ &+F\,|\,x_4-x_{\mathrm{c}}\,|+F'\,|\,x_5-x_{\mathrm{c}}\,|-F'\,|\,x_6-x_{\mathrm{c}}\,|.\end{aligned} \tag{10}$$

According to Eqs. (4)–(8), F, F', and M are functions of t; when F and F' are at their maximum values, we can optimize M to its minimum value, and subsequently the angular velocities reach their minimum values. This provides the theoretical evidence for the optimization of angular velocities for separation.

3 Optimization method

Due to the limited energy on a pico-satellite, its attitude control ability is poor. The attitude control subsystem imposes some corresponding requirements on the initial attitude for the satellite to be placed into orbit. The detailed requirements are listed in Table 1.

Table 1 Technical indices of the pico-satellite satellite–rocket separation

No.	Technical specification	Design value
1	Separation velocity (m/s)	v=1±0.1
2	Mass of separation mechanism (kg)	m≤4.5
3	Rolling angular velocity (°/s)	$\|\Delta w_\gamma\|$≤2
4	Pitch velocity (°/s)	$\|\Delta w_\phi\|$≤2
5	Yaw velocity (°/s)	$\|\Delta w_\psi\|$≤2

3.1 Initial separation parameter analysis

The mass characteristics of the pico-satellite are provided in Table 2. As shown in Fig. 4, the entire separation system was used as inputs in the ADAMS software to obtain the angular velocities of satellite separation when the spring pushing rods and position switches were in their original positions, and the external moments were calculated according to Eqs. (9) and (10). The calculation and simulation results are provided in Table 3.

Table 2 Pico-satellite mass characteristics

Characteristic	Value
Satellite mass (kg)	24.328
Mass center (mm)	(13.397, 11.165, 243.348)
Moment of inertia (kg·m^2)	I_x=1.098; I_y=1.124; I_z=0.416

From Table 3, it can be observed that ω_x and ω_y are far beyond the technical specifications; therefore, we need to optimize ω_x and ω_y to meet the requirements.

3.2 Angular velocity optimization

Based on the analysis provided in Section 3.1 which demonstrates the evident influence of the positions of the pushing rods on the external moment and angular velocities, we first established the data relations between various factors, the external moments, and angular velocities by developing four optimization steps to optimize the target values. If the current step cannot complete the optimization, the next step will be adjusted accordingly, until the external moments and angular velocities are optimized to the minimum. The optimization process is shown in Fig. 6.

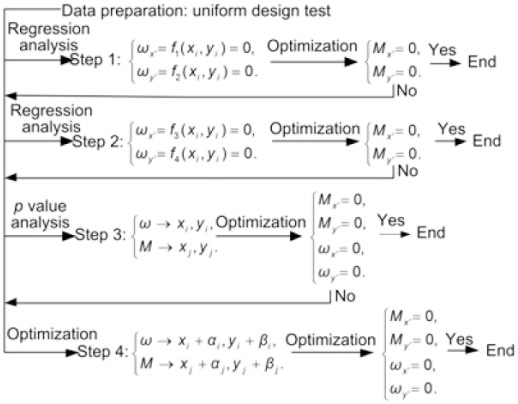

Fig. 6 Optimization process

3.2.1 Data preparation

In the multi-factor test, more factors and levels cause an exponential increase in the number of tests that must be conducted. Consider the orthogonal test as an example: It requires 27 tests for 12 factors and 3 levels. For 8 factors and 5 levels, 49 tests are required. However, for 12 factors and 13 levels, orthogonal tests cannot be created.

Table 3 External moments and separation angular velocities before optimization

Coordinate value (mm)											
x_1	y_1	x_2	y_2	x_3	y_3	x_4	y_4	x_5	y_5	x_6	y_6
0	118.5	118.5	0	0	−118.5	−118.5	0	−50	108.8	50	−108.5

External moment (N·m)			Angular velocity (°/s)		
M_x	M_y	M_z	ω_x	ω_y	ω_z
−7.677	9.217	0	16.729	−13.105	−1.598

A uniform design can solve the multi-factor and multi-level problems, and requires fewer test combinations to obtain the influence of each factor on the target value or even determine the value of each factor when it arrives at a satisfactory target value.

According to the contact ranges among the pushing rods, position switches, and the satellite, we chose the boundary positions of the pushing rods and position switches as the constraint conditions for the coordinates. We selected the relative position coordinates for the four pushing rods and two position switches, and considered them as the factors for optimization; thus, $M_{x'}$, $M_{y'}$, $\omega_{x'}$, and $\omega_{y'}$ are the optimization targets. We established a parameter level table for the position coordinates of the spring pushing rods and position switches (Table 4).

Excluding the interactive function of all factors, we established 12 factors and 13 levels for the uniform design test table. By calculating the external moments and simulating the separation processes, we obtained the external moments and angular velocities for 13 schemes (Table 5).

3.2.2 Step 1

Most of the test designs use the variance and regression analysis methods to process data. The data of the uniform design test are too few to realize variance analysis. Thus, regression analysis is the main analysis method. If the factor level L is greater than $(q+1)(q+2)/2$ (where q is the number of factors), quadratic regression analysis can be used. Hence, this study uses only linear regression analysis.

The coefficients of the multiple linear regression equation can be obtained by derivation of equations. Leng et al. (2016) used the multiple linear regression method to analyze the civil aviation passenger volume, and established a prediction model for civil aviation passenger volume.

We introduce a token proposed by Leng et al. (2016):

$$\begin{cases} l_{uv}=l_{vu}=\sum\limits_{a=1}^{n}(x_{ua}-\overline{x}_u)(x_{va}-\overline{x}_v), \\ l_{uy}=\sum\limits_{a=1}^{n}(x_{ua}-\overline{x}_u)(y_a-\overline{w}), \end{cases} \tag{11}$$

where u, v=1, 2, …, q, x is the coordinate value, w represents the angular velocity and external moment, n is the number of uniform tests, x_{ua} and x_{va} are the values of x in the u^{th}, v^{th} rows and the a^{th} column, respectively, $\overline{x}_u$ and $\overline{x}_v$ are the means of x in the u^{th} and v^{th} columns, respectively, and $\overline{w}$ is the mean of w.

Then the normal equations can be rewritten as

$$\begin{cases} l_{11}b_1+l_{12}b_2+\cdots+l_{1v}b_v=l_{1y}, \\ l_{21}b_1+l_{22}b_2+\cdots+l_{2v}b_v=l_{2y}, \\ \quad\vdots \\ l_{u1}b_1+l_{u2}b_2+\cdots+l_{uv}b_v=l_{uy}, \\ b_0=\overline{y}-b_1\overline{x}_1-b_2\overline{x}_2-\cdots-b_u\overline{x}_u, \end{cases} \tag{12}$$

where l_{uv} and l_{uy} are shown in Table 6, and b_0, b_1, ..., b_k can be determined by solving Eq. (12). Then the regression equation can be established.

The multiple linear regression equation can also

Table 4 Parameter level table

Level	Coordinate value (mm)											
	x_1	y_1	x_2	y_2	x_3	y_3	x_4	y_4	x_5	y_5	x_6	y_6
1	−6	112.5	112.5	−6	−6	−124.5	−124.5	−6	−56	102.5	44	−114.5
2	−5	113.5	113.5	−5	−5	−123.5	−123.5	−5	−55	103.5	45	−113.5
3	−4	114.5	114.5	−4	−4	−122.5	−122.5	−4	−54	104.5	46	−112.5
4	−3	115.5	115.5	−3	−3	−121.5	−121.5	−3	−53	105.5	47	−111.5
5	−2	116.5	116.5	−2	−2	−120.5	−120.5	−2	−52	106.5	48	−110.5
6	−1	117.5	117.5	−1	−1	−119.5	−119.5	−1	−51	107.5	49	−109.5
7	0	118.5	118.5	0	0	−118.5	−118.5	0	−50	108.5	50	−108.5
8	1	119.5	119.5	1	1	−117.5	−117.5	1	−49	109.5	51	−107.5
9	2	120.5	120.5	2	2	−116.5	−116.5	2	−48	110.5	52	−106.5
10	3	121.5	121.5	3	3	−115.5	−115.5	3	−47	111.5	53	−105.5
11	4	122.5	122.5	4	4	−114.5	−114.5	4	−46	112.5	54	−104.5
12	5	123.5	123.5	5	5	−113.5	−113.5	5	−45	113.5	55	−103.5
13	6	124.5	124.5	6	6	−112.5	−112.5	6	−44	114.5	56	−102.5

Table 5 Uniform design test table, calculation and simulation results

Level	Coordinate value (mm)											
	x_1	y_1	x_2	y_2	x_3	y_3	x_4	y_4	x_5	y_5	x_6	y_6
1	2	6	11	11	2	9	13	6	5	7	1	10
2	5	3	7	9	12	10	4	2	2	12	9	5
3	8	13	12	1	8	11	7	4	7	9	13	12
4	13	4	1	10	5	8	3	7	9	4	10	13
5	6	8	9	13	6	5	10	3	12	3	11	2
6	12	5	10	5	7	12	8	10	3	1	5	1
7	1	11	5	7	4	13	2	11	11	8	7	3
8	10	7	13	12	9	1	5	13	8	13	6	8
9	7	2	4	4	1	4	11	12	6	10	12	6
10	9	9	6	2	3	3	1	1	4	5	3	7
11	4	1	8	3	13	6	6	9	13	6	4	11
12	11	10	2	6	11	7	12	5	10	11	2	4
13	3	12	3	8	10	2	9	8	1	2	8	9

Level	External moment (N·m)			Angular velocity (°/s)		
	$M_{x'}$	$M_{y'}$	$M_{z'}$	$\omega_{x'}$	$\omega_{y'}$	$\omega_{z'}$
1	−6.977	9.345	0	12.869	−14.825	−0.508
2	−8.289	9.265	0	16.351	−13.346	−0.799
3	−7.405	7.973	0	14.567	−9.346	0.902
4	−7.469	10.121	0	15.124	−16.547	−0.684
5	−7.662	8.581	0	15.986	−11.658	−0.752
6	−7.217	7.837	0	13.234	−8.465	−0.814
7	−5.433	11.777	0	10.347	−19.436	−0.883
8	−6.749	7.741	0	11.358	−7.965	−0.547
9	−8.633	9.973	0	17.632	−15.435	−0.766
10	−9.845	10.805	0	20.355	−18.125	−2.006
11	−9.109	8.677	0	18.952	−12.135	−0.471
12	−7.665	7.937	0	16.012	−9.012	−0.905
13	−7.401	9.789	0	14.134	−14.567	−0.298

be solved using EXCEL, SPSS, SAS, and other data analysis software. Fritz and Berger (2015) discussed the method of establishing a multiple linear regression model using EXCEL. Using the regression analysis function in EXCEL, data analysis, partial regression coefficient, coefficient of variation (R^2), standard error, and other parameters can be obtained directly. The specific solution process can be seen in Fritz and Berger (2015).

Therefore, the linear regression equation for $\omega_{x'}$ and $\omega_{y'}$ can be expressed as

$$\begin{cases} \omega_{x'} = 35.773 - 0.026x_1 - 0.393y_1 - 0.1x_2 - 0.431y_2 \\ \qquad - 0.011x_3 - 0.374y_3 + 0.031x_4 - 0.472y_4 \\ \qquad + 0.119x_5 - 0.05y_5 + 0.036x_6 - 0.062y_6, \end{cases} \tag{13}$$

$$\begin{cases} \omega_{y'} = -45.903 + 0.499x_1 + 0.094y_1 + 0.479x_2 \\ \qquad - 0.019y_2 + 0.53x_3 + 0.007y_3 + 0.427x_4 \\ \qquad + 0.108y_4 + 0.029x_5 + 0.037y_5 + 0.067x_6 \\ \qquad - 0.096y_6. \end{cases} \tag{14}$$

Using the method of nonlinear least squares (Hu et al., 2012), we optimize $\omega_{x'}$ and $\omega_{y'}$ to 0°/s. The nonlinear least squares can be expressed as

$$S(\boldsymbol{\gamma}) = \sum_{i=1}^{\lambda} \left[Y_i - f(x_i, \boldsymbol{\gamma}) \right]^2, \tag{15}$$

where $\boldsymbol{\gamma}$ is the parameter vector, Y_i is the empirical value, λ is the number of empirical values, $f(x_i, \boldsymbol{\gamma})$ is the optimized function, and $S(\boldsymbol{\gamma})$ is the sum of the quadratic error functions.

The optimization results of the regression and polynomial optimization are shown in Figs. 7 and 8. From Figs. 7 and 8, it can be seen that Eq. (13) cannot be optimized to 0; when Eq. (14) is optimized to 0, $M_{x'}$ and $M_{y'}$ are not 0. The optimization results are provided in Table 7. It indicates that step 1 cannot complete the optimization.

3.2.3 Step 2

From Eq. (4) we know that $\omega_{x'}$ is related to only

Table 6 Values of l_{uv}, l_{uy_1}, and l_{uy_2}

v	l_{uv}												l_{uy_1}	l_{uy_2}
	u=1	u=2	u=3	u=4	u=5	u=6	u=7	u=8	u=9	u=10	u=11	u=12		
1	182	−20	−17	−19	7	−18	−19	−5	−2	−5	10	0	21.809	76.618
2	−20	182	4	−16	−3	7	−2	−41	−13	−13	8	−10	−47.795	3.166
3	−17	4	182	15	9	17	15	9	−3	28	−9	1	−38.199	91.246
4	−19	−16	15	182	−5	−31	31	14	16	3	−1	−25	−63.971	7.515
5	7	−3	9	−5	182	−8	−9	−18	14	31	−15	11	10.370	97.730
6	−18	7	17	−31	−8	182	−17	−16	10	−7	8	−35	−47.626	−7.679
7	−19	−2	15	31	−9	−17	182	14	−5	−3	−18	−22	−7.8175	71.898
8	−5	−41	9	14	−18	−16	14	182	30	19	4	−5	−66.989	16.058
9	−2	−13	−3	16	14	10	−5	30	182	22	3	4	0.740	10.513
10	−5	−13	28	3	31	−7	−3	19	22	182	4	11	−12.724	33.282
11	10	8	−9	−1	−15	8	−18	4	3	4	182	17	−1.662	−2.973
12	0	−10	1	−25	11	−35	−22	−5	4	11	17	182	18.530	−20.139

Table 7 Optimization results of regression polynomials ω_x and ω_y (Eqs. (13) and (14))

Angular velocity (°/s)	Coordinate value (mm)												External moment (N·m)	
	x_1	y_1	x_2	y_2	x_3	y_3	x_4	y_4	x_5	y_5	x_6	y_6	$M_{x'}$	$M_{y'}$
ω_x=2.588	6	124.500	124.500	6.000	0	−112.5	−124.500	6.000	−56.000	114.500	44.000	−102.500	−3.554	8.425
ω_y=0	6	124.488	124.497	−1.309	5.906	−112.5	−112.502	5.994	−54.315	111.568	52.849	−111.445	−5.116	5.256

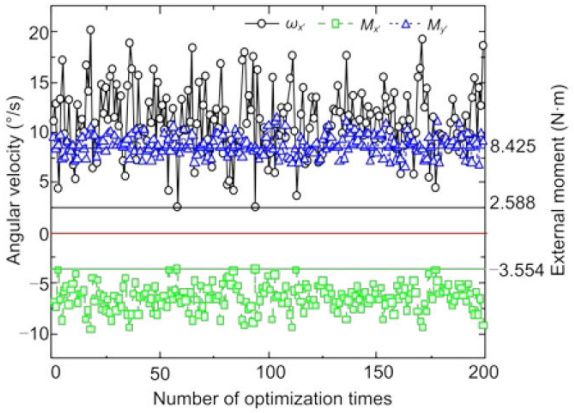

Fig. 7 Optimization results of regression polynomial $\omega_{x'}$

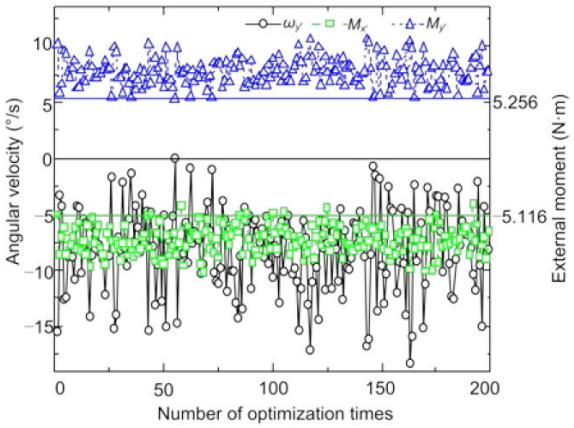

Fig. 8 Optimization results of regression polynomial $\omega_{y'}$

coordinate value y, and $\omega_{y'}$ is related to only coordinate value x. Therefore, we eliminate the factors irrelevant to the target values, and obtain two other regression equations for $\omega_{x'}$ and $\omega_{y'}$:

$$\begin{cases}\omega_{x'} = 17.472 - 0.394y_1 - 0.422y_2 - 0.372y_3 \\ \qquad - 0.453y_4 + 0.055y_5 - 0.058y_6, \end{cases} \tag{16}$$

$$\begin{cases}\omega_{y'} = -20.281 + 0.489x_1 + 0.489x_2 + 0.518x_3 \\ \qquad + 0.439x_4 + 0.042x_5 + 0.066x_6. \end{cases} \tag{17}$$

The regression polynomial can be optimized again; the optimization results are shown in Figs. 9 and 10. Eq. (17) cannot be optimized to 0; when Eq. (16) is optimized to 0, $M_{x'}$ and $M_{y'}$ are still not 0. The optimization results are provided in Table 8. It shows that the adjusted step 2 still cannot complete the optimization.

3.2.4 Step 3

The optimization results show that in the polynomial regression Eqs. (13), (14), (16) and (17) in steps 1 and 2, the relationship between the coordinates and angular velocities ($\omega_{x'}$, $\omega_{y'}$) cannot be applied directly. Eqs. (5)–(10) show that $M_{x'}$ and $M_{y'}$ are related to the coordinates directly; however, we need to know which factors influence the target values significantly. To determine the influence of each factor on the target value, we must analyze the statistic of

Table 8 Optimization results of regression polynomials $\omega_{x'}$ and $\omega_{y'}$ after eliminating the irrelevant factors (Eqs. (16) and (17))

Angular velocity (°/s)	Coordinate value (mm)												External moment (N·m)	
	x_1	y_1	x_2	y_2	x_3	y_3	x_4	y_4	x_5	y_5	x_6	y_6	$M_{x'}$	$M_{y'}$
$\omega_{x'}$=2.588	–	113.818	–	4.627	–	−114.998	–	3.134	–	107.954	–	−102.5	−3.523	–
$\omega_{y'}$=0	6	–	124.5	–	6	–	−112.5	–	−44	–	56	–	–	5.089

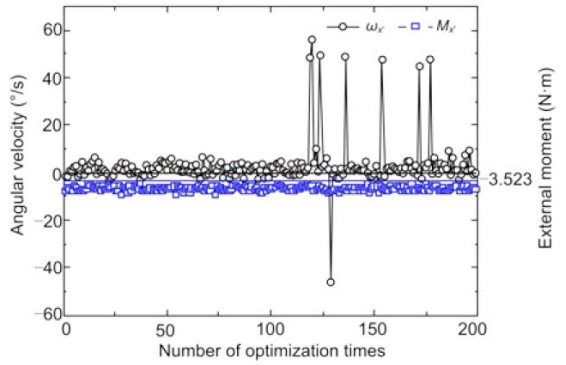

Fig. 9 Optimization results of regression polynomial $\omega_{x'}$ after eliminating the irrelevant factors

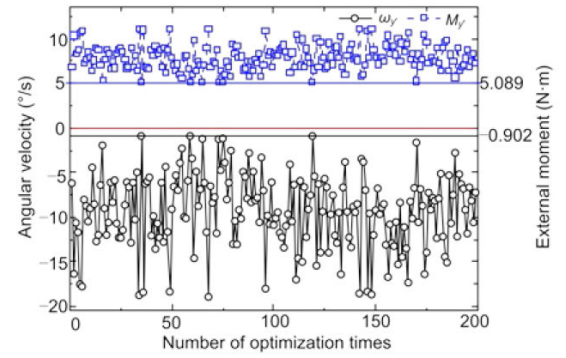

Fig. 10 Optimization results of regression polynomial $\omega_{y'}$ after eliminating the irrelevant factors

regression coefficient, i.e., p value analysis. When p value is lower than significance level 0.05, indicating that the factors are related to the target value, a lower p value indicates a stronger effect on the target value. The analysis results are shown in Tables 9 and 10.

From Tables 9 and 10, we can obtain the effect of the p values of six factors on $\omega_{x'}$, $\omega_{y'}$, $M_{x'}$, and $M_{y'}$. The orders of the six factors affecting $\omega_{x'}$ and $M_{x'}$ are $y_4>y_2>y_1>y_3>y_6>y_5$ and $y_1>y_2>y_4>y_3>y_5>y_6$, respectively. The orders of the six factors affecting $\omega_{y'}$ and $M_{y'}$ are $x_3>x_2>x_1>x_4>x_6>x_5$ and $x_2>x_3>x_1>x_4>x_5>x_6$, respectively. From the p value analysis, we know that $\omega_{x'}$, $\omega_{y'}$, $M_{x'}$, and $M_{y'}$ cannot be optimized when the position of only one pushing rod is changed. When the positions of only two pushing rods are changed in the separation mechanism, the effect on the separation mechanism is less. Therefore, x_i, x_j, y_i, and y_j can be obtained, i.e., $x_i=x_3$, $x_j=x_2$, $y_i=y_4$, and $y_j=y_1$. Therefore, we chose two sets of coordinates (y_4, x_3 and y_1, x_2) to optimize $M_{x'}$ and $M_{y'}$, respectively. The original optimization results of $M_{x'}$ and $M_{y'}$ can be found in Table 11, and the optimization results are shown in Fig. 11. From Table 11, we can see that $M_{x'}$ and $M_{y'}$ have been optimized in limited coordinate ranges; however, $M_{x'}$ and $M_{y'}$ cannot be optimized to 0.

Table 9 Analysis results of the p value for $\omega_{x'}$ and $\omega_{y'}$

Factor	p value for $\omega_{x'}$	Factor	p value for $\omega_{y'}$
y_1	0.001 191	x_1	0.000 373
y_2	0.000 854	x_2	0.000 371
y_3	0.001 716	x_3	0.000 273
y_4	0.000 584	x_4	0.000 681
y_5	0.445 332	x_5	0.555 402
y_6	0.429 651	x_6	0.368 524

Table 10 Analysis results of the p value for $M_{x'}$ and $M_{y'}$

Factor	p value for $M_{x'}$	Factor	p value for $M_{y'}$
y_1	8.40×10^{-93}	x_1	6.71×10^{-93}
y_2	8.56×10^{-93}	x_2	6.64×10^{-93}
y_3	8.97×10^{-93}	x_3	6.68×10^{-93}
y_4	8.58×10^{-93}	x_4	6.84×10^{-93}
y_5	8.45×10^{-87}	x_5	7.45×10^{-87}
y_6	1.02×10^{-86}	x_6	7.76×10^{-87}

3.2.5 Step 4

From the optimization results in step 3, we know that if the external moments need to be optimized, the coordinate ranges of y_4, x_3 and y_1, x_2 must be enlarged; however, the minimum external moments have the following constraints:

$$\begin{cases} M_{x'} = F\,|y_1-y_c| - F\,|y_2-y_c| - F\,|y_3-y_c| \\ \qquad + F\,|y_4-y_c| + F'\,|y_5-y_c| - F'\,|y_6-y_c|, \end{cases} y_4>y_c, \quad (18)$$

$$\begin{cases} M_{y'} = F\,|x_1-x_c| - F\,|x_2-x_c| - F\,|x_3-x_c| \\ \qquad + F\,|x_4-x_c| + F'\,|x_5-x_c| - F'\,|x_6-x_c|, \end{cases} x_3>x_c. \quad (19)$$

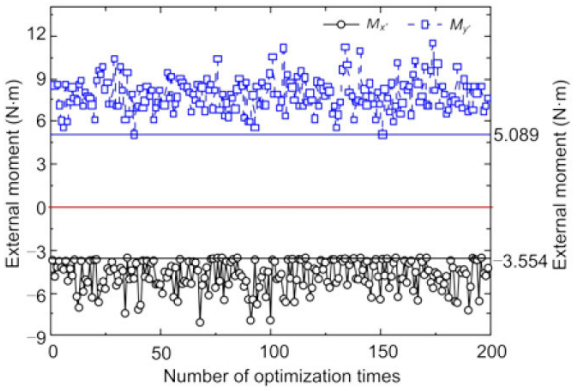

Fig. 11 The original optimization results for $M_{x'}$ and $M_{y'}$

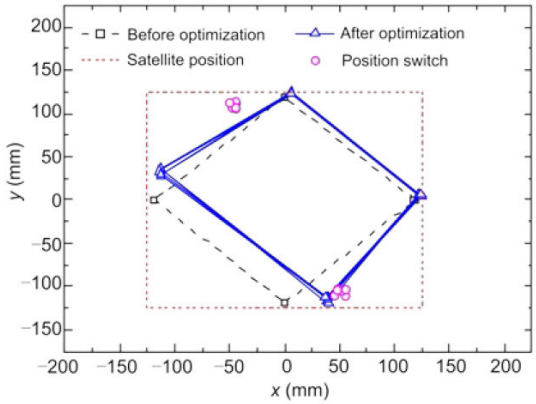

Fig. 12 Relative positions of elastic devices when enlarging the coordinate ranges of y_4 and x_3

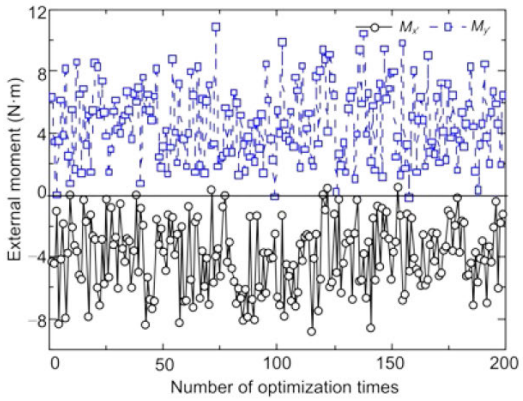

Fig. 13 One of the optimization results when enlarging the coordinate ranges of y_4 and x_3

First, we expanded the coordinate value for y_4 and x_3 to make $M_{x'}$ and $M_{y'}$ reach the target values; y_4 was changed from [−6, 6] to [−6, 36], i.e., β_i=β_4=30, and x_3 was changed from [−6, 6] to [−6, 40], i.e., α_i=α_3=34. When $M_{x'}$ and $M_{y'}$ are optimized to the target values, many similar optimization results are obtained (Fig. 12). One of the optimization results is shown in Fig. 13. The final optimization results are shown in Table 12; this time, $M_{x'}$ and $M_{y'}$ reach 0 N·m, and $\omega_{x'}$ and $\omega_{y'}$ reach the minimum values.

When y_1 and x_2 are expanded, y_1 changed from [112.5, 124.5] to [112.5, 150.5], i.e., β_j=β_1=26, and x_2 changed from [112.5, 124.5] to [112.5, 160.5], i.e., α_j=α_2=36. When $M_{x'}$ and $M_{y'}$ are optimized to the target values, many optimization results are obtained (Fig. 14). However, it can be found from Fig. 14 that the optimized positions of pushing rods 1 and 2 exceed the envelope of the satellite, and that not all the optimization results can be adopted. Therefore, the optimization results that change pushing rods 3 and 4 were adopted.

4 Test preparation

The arrangement of springs on the separation mechanism was changed based on the optimization results in Table 12. However, according to the results

Table 11 Original optimization results of external moments

Coordinate value (mm)												External moment (N·m)		
x_1	y_1	x_2	y_2	x_3	y_3	x_4	y_4	x_5	y_5	x_6	y_6	$M_{x'}$	$M_{y'}$	$M_{z'}$
6	124.5	124.5	6	6	−112.5	−112.5	6	−44	114.5	56	−102.5	−3.554	5.089	0

Table 12 Final optimization results of external moment and separation angle velocities

Coordinate value (mm)											
x_1	y_1	x_2	y_2	x_3	y_3	x_4	y_4	x_5	y_5	x_6	y_6
5.999	124.487	124.427	6	37.171	−112.811	−112.528	29.108	−44.002	111.741	55.604	−111.185

External moment (N·m)			Angular velocity (°/s)		
$M_{x'}$	$M_{y'}$	$M_{z'}$	$\omega_{x'}$	$\omega_{y'}$	$\omega_{z'}$
0	0	0	−0.874	0.086	−0.063

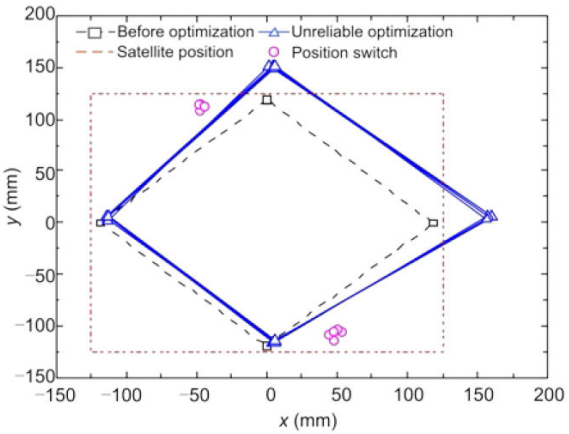

Fig. 14 Relative positions of elastic devices when enlarging the coordinate ranges of y_1 and x_2

in Table 12, there will be an overlap between the positions of spring sleeve 4 and position switch 2. Because the effect of the spring force of the separation spring is greater than that of the position switch, position switch 2 can be moved 8 mm away from spring sleeve 4. The positions of the pushing rods and position switches are shown in Fig. 15.

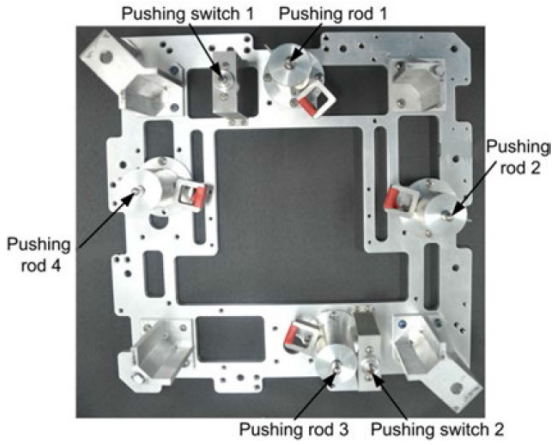

Fig. 15 Positions of pushing rods and position switches

By establishing a test system that can offset gravity (Fig. 16), we carried out the separation test and obtained the separation parameters. The test system includes a pico-satellite, a satellite–rocket separation mechanism, a high-speed camera, a three-axis angular velocity sensor, a hanging rack, a roller hook, a synchronized unlocking device, and tools. The high-speed camera was used to measure the separation velocity and observe whether the separation is steady. The three-axis angular velocity sensor was used to measure the angular velocities of the three axes during separation. The hanging rack was used to offset gravity, and the roller hook reduced the separation resistance. The synchronized unlocking device was used to realize synchronous unlocking.

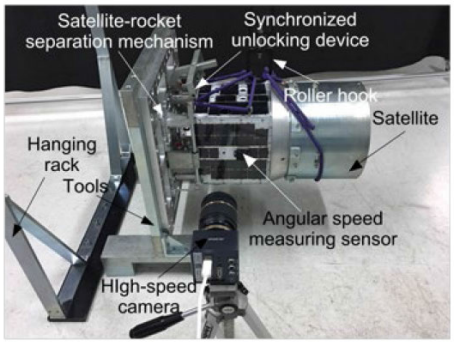

Fig. 16 Offset gravity test system before separation

5 Results and discussion

The comparison of the simulation results before and after optimization is shown in Fig. 17. It can be seen that the angular velocities are improved greatly. Moreover, it can be seen from Fig. 17 that the effect on separation can be ignored after moving position switch 2. The optimization results satisfy the separation requirements.

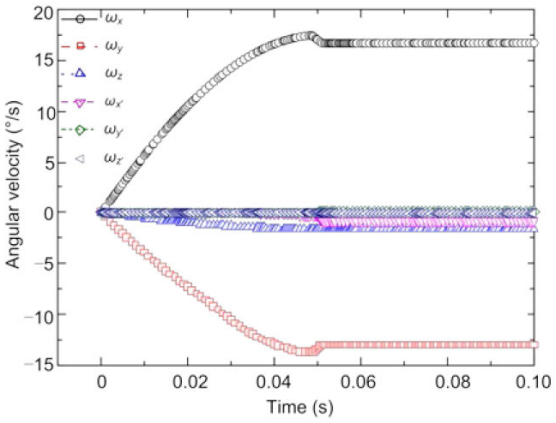

Fig. 17 Comparison of the simulation results before and after optimization

The separation results and comparison of the simulation results after optimization and testing are

shown in Figs. 18 and 19, respectively. The results show that the separation angle velocities are improved greatly, and that the test results are close to the optimization results. The optimization and test results are shown in Table 13. There are four main reasons for the deviation of the actual measurements of the angular velocities from the simulation results. First, there are minor deviations between the characteristics, such as spring length and stiffness between the separation springs when selected. Second, the actual measurement of the mass center of the satellite can deviate; generally, the deviation is approximately 1%–5%, whereas the deviated mass center of the satellite is used in the simulation generally. Third, the friction coefficient and friction direction in the simulation are different from those in a real situation. Finally, the satellite is subject to shock by synchronized unlocking at the moment of unlocking (Fig. 19).

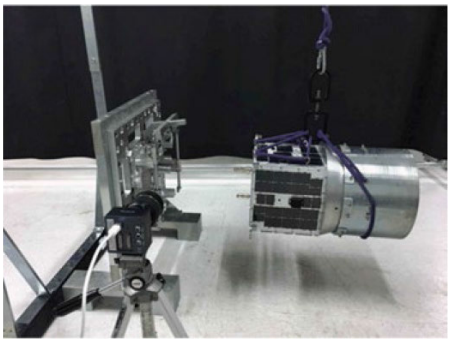

Fig. 18 Offset gravity test system after separation

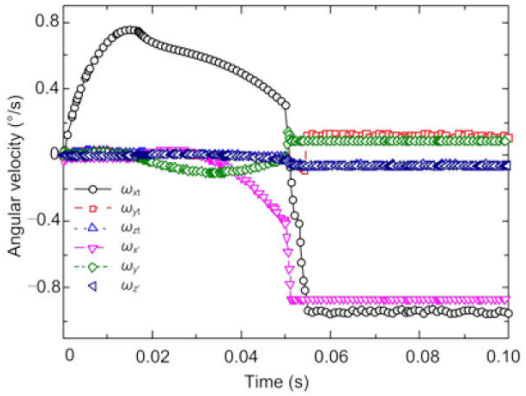

Fig. 19 Comparison of the simulation results after optimization and testing
Variables with subscript t refer to the tested results

Thousands of ground separation tests proved that the satellite can separate successfully. The satellite separates steadily without any hooking or interference on the satellite–rocket separation mechanism. Thus, the test results show that the separation accuracy satisfies the separation requirements.

Table 13 Comparison of optimization and test results

Technical specification	Simulation result	Test result	Relative error (%)
Time (s)	0.051	0.055	7.27
Separation velocity (m/s)	0.980	1.050	7.14
Rolling angular velocity (°/s)	−0.063	−0.075	19.04
Pitch velocity (°/s)	0.086	0.100	16.27
Yaw velocity (°/s)	−0.874	−0.960	9.84

When the positions of the elastic devices are not in a wide-range limitation, the external moments can always be optimized to the minimum values. The relative positions of the pushing rods and position switches are shown in Fig. 20. However, the installation ranges of the elastic devices are limited for a separation mechanism. Therefore, these optimization results are unreliable. The main reason for these results is that the major factors affecting the deviation of angular velocities have not been found.

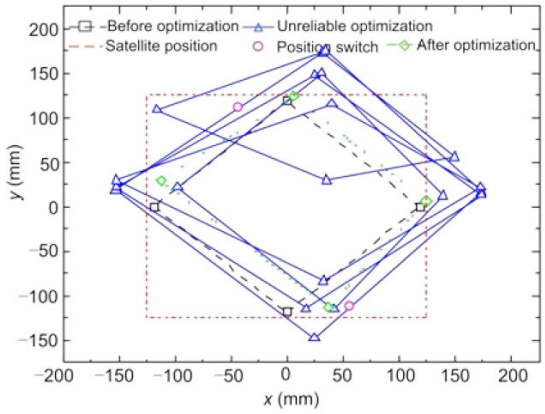

Fig. 20 Relative positions of elastic devices when the coordinate ranges are not in a wide-range limitation

Without considering the influence of friction force, the separation of the satellite is determined by the mass center of the satellite and the installation positions of the elastic devices. The mass center of the spacecraft will be adjusted before launch to benefit its attitude control and steady separation; however, it is difficult to adjust for no eccentricity. The deviation in the angular velocities of satellite separation is caused directly by external moments. When the external

moments can be optimized, they should be optimized on priority. However, the main factors affecting the deviation of angular velocities may have to be determined using an angular velocity optimization method; the angular velocities can also be optimized according to the different positions of elastic devices to some extent. In addition, the composite optimization method can be used to combine the angular velocities with external moments to optimize the angular velocities of the spacecraft.

6 Conclusions

In this paper, a composite optimization method which combines the angular velocities with external moments for the separation parameters of large-eccentricity pico-satellites was proposed. By changing the positions of elastic launch devices, this method effectively controls the popping process with less change in the separation mechanism. The reasons for the deviation of the angular velocities and the unreliable optimization results were presented and analyzed. This optimization method was proved through a ground test, in which the gravity was offset. This method was adaptable particularly to non-stable elastic parameters, distribution of all kinds of elastic devices, and large-eccentricity spacecraft for which attitude correction is difficult. The separation accuracy of a satellite was improved greatly using this optimization method. It can avoid the over-large separation angular velocities that are beyond the control scope of satellite attitude. A solid foundation was thus laid for attitude control. Meanwhile, this provides a solution for large-eccentricity spacecraft and bad separation attitudes.

References

Chao J, Wang ZK, Zhang YL, 2015. Development of the new approach of formation initialization using spring separation mechanism considering J_2 perturbation. *Adv Space Res*, 55(11):2616-2627. https://doi.org/10.1016/j.asr.2015.02.019

Cui DL, Yan SZ, Li JL, et al., 2014. Dynamic analysis of satellite separation considering the flexibility of interface rings. *J Aerosp Eng*, 229(10):1886-1902. https://doi.org/10.1177/0954410014562012

Cui DL, Zhao JL, Yan SZ, et al., 2015. Analysis of parameter sensitivity on dynamics of satellite separation. *Acta Astronaut*, 114(3):22-33. https://doi.org/10.1016/j.actaastro.2015.04.007

Fritz M, Berger PD, 2015. Can you relate in multiple ways? Multiple linear regression and stepwise regression. In: Kaufmann M (Ed.), Improving the User Experience Through Practical Data Analytics. Elsevier Inc., Boston, p.239-269. https://doi.org/10.1016/B978-0-12-800635-1.00010-0

Hu J, Li HC, Zhou YP, 2012. The application of Levenberg-Marquardt algorithm in the image stitching. *Telecom Mark*, 2:149-154 (in Chinese). https://doi.org/10.3969/j.issn.1006-6675-B.2012.02.049

Hu XZ, Chen XQ, Tuo ZH, et al., 2013. Dynamics and transient perturbation analysis of satellite separation systems. *Proc Inst Mech Eng G*, 227(12):1968-1976. https://doi.org/10.1177/0954410012466780

Hu XZ, Chen XQ, Zhao Y, et al., 2014a. Optimization design of satellite separation systems based on multi-island genetic algorithm. *Adv Spac Res*, 53(5):870-876. https://doi.org/10.1016/j.asr.2013.12.021

Hu XZ, Chen XQ, Tuo ZH, et al., 2014b. Simplified metrics of elastic potential energy for spacecraft separation dynamics. *Acta Astronaut*, 102:151-155. https://doi.org/10.1016/j.actaastro.2014.05.028

Hu XZ, Chen XQ, Zhao Y, et al., 2017. Active subspace approach to reliability and safety assessments of small satellite separation. *Acta Astronaut*, 131:159-165. https://doi.org/10.1016/j.actaastro.2016.10.042

Huang WH, Cao DQ, Han ZY, 2012. Advances and trends in dynamics and control of spacecrafts. *Adv Mech*, 42(4): 367-394. https://doi.org/10.6052/1000-0992-11-171

Iwasa T, Shi Q, Ando S, et al., 2007. Simplified SRS prediction method for pyroshock source of V-band clamp separation devices. 48th AIAA/ASME/ASCE/AHS/ASC Structures, Structural Dynamics, and Materials Conf, p.1-12. https://doi.org/10.2514/6.2007-2020

Jiang C, Wang ZK, Zhang YL, 2015. Angular velocity depressing method of constrained and centroid biased on-orbit separation. *Acta Aeronaut Astronaut Sin*, 36(10): 3382-3392 (in Chinese). https://doi.org/10.7527/S1000-6893.2015.0093

Jing C, Wang ZK, Fan L, et al., 2010. Dynamics analysis of the constrained and centroid biased on-orbit satellite separation. *Flight Dynam*, 28(1):76-79 (in Chinese). https://doi.org/10.13645/j.cnki.f.d.2010.01.014

Lan W, Brown J, Toorian A, et al., 2006. CubeSat development in education and into industry. AIAA SPACE Forum, Article 7296. https://doi.org/10.2514/6.2006-7296

Leng JF, Gao X, Zhu JP, 2016. Application of multivariate linear regression statistical prediction model. *Stat Dec*, 7:82-85 (in Chinese). https://doi.org/10.13546/j.cnki.tjyjc.2016.07.021

Li JL, Yan SZ, Tan XF, 2012. Modeling and simulation of clamp band dynamic envelope in a LV/SC separation system. *Appl Mech Mater*, 141:359-363. https://doi.org/10.4028/www.scientific.net/AMM.141.359

Li JL, Yan SZ, Tan XF, 2014. Dynamic-envelope analysis of

clamp-band joint considering pyroshock of satellite separation. *J Spacecr Rock*, 51(5):1390-1400. https://doi.org/10.2514/1.A32382

Michaels D, Gany A, 2016. Modeling and testing of a tube-in-tube separation mechanism of bodies in space. *Acta Astronaut*, 129:214-222. https://doi.org/10.1016/j.actaastro.2016.09.013

Miyamoto K, Ui K, Miyashita S, et al., 2005. Tokyo tech separation demonstration TSD as M-V rocket sub-payload for nanosatellite separation mechanism. 56th Int Astronautical Congress of the Int Astronautical Federation, the Int Academy of Astronautics, and the Int Institute of Space Law, Article IAC-05-B5.6.A. https://doi.org/10.2514/6.IAC-05-B5.6.A.03

Paris C, 2015. Vibration tests on the preloaded LARES satellite and separation system. *Aerosp Sci Technol*, 42: 470-476. https://doi.org/10.1016/j.ast.2015.01.023

Qin ZY, Yan SZ, Chu FL, 2009. Axial stiffness analysis of clamp band system. *J Astron*, 30(5):2080-2085 (in Chinese). https://doi.org/10.3873/j.issn.1000-1328.2009.05.056

Qin ZY, Yan SZ, Chu FL, 2010. Dynamic analysis of clamp band joint system subjected to axial vibration. *J Sound Vib*, 329(21):4486-4500 https://doi.org/10.1016/j.jsv.2010.05.012

Qin ZY, Yan SZ, Chu FL, 2011. Dynamic characteristics of launch vehicle and spacecraft connected by clamp band. *J Sound Vib*, 330(10):2161-2173. https://doi.org/10.1016/j.jsv.2010.06.011

Qin ZY, Yan SZ, Chu FL, 2012. Finite element analysis of the clamp band joint. *Appl Math Model*, 36(1):463-477. https://doi.org/10.1016/j.apm.2011.07.022

Qin ZY, Yan SZ, Chu FL, 2014. Influence of clamp band joint on dynamic behavior of launching system in ascent flight. *J Aerosp Eng*, 228(1):97-114. https://doi.org/10.1177/0954410012468070

Singaravelu J, Jeyakumar D, Rao BN, 2011. Reliability and safety assessments of the satellite separation process of a typical launch vehicle. *J Def Model Simul: Appl Method Technol*, 9(4):369-382. https://doi.org/10.1177/1548512911401939

Somanath S, Krishnan Kutty VK, Francis EJ, et al., 2001. Dynamics simulation of pyro actuated "ball lock" separation system for microsatellites to evaluate release shock. 9th European Space Mechanisms and Tribology Symp, p.199-206.

Tan XF, Yan SZ, 2010. Dynamic simulation and failure analysis of a clamp band system for spacecraft. *J Tsinghua Univ (Sci Tech)*, 50:1205-1209 (in Chinese). https://doi.org/10.16511/j.cnki.qhdxxb.2010.08.012

Tayefi M, Ebrahimi M, 2009. Design and analysis of separation systems based on an optimization approach. 47th AIAA Aerospace Sciences Meeting Including the New Horizons Forum and Aerospace Exposition, p.436-445. https://doi.org/10.2514/6.2009-436

Teng L, Jin ZH, 2016. Pico-satellite separation parameters optimization. *J Astronaut*, 37(10):1200-1206 (in Chinese). https://doi.org/10.3873/j.issn.1000-1328.2016.10.007

Wang QM, Meng XH, Yang QC, 2010. Research of simulation on programs of satellite secondary separation. *J Syst Simul*, 9(22):2217-2222 (in Chinese). https://doi.org/10.16182/j.cnki.joss.2010.09.010

Wu CJ, Xu XQ, 2014. New cage style pico-satellite deployer based on sliding guide structure. *J Zhejiang Univ (Eng Sci)*, 48(3):548-554 (in Chinese). https://doi.org/10.3785/j.issn.1008-973X.2014.03.025

Wu CJ, Xu XQ, He XE, et al., 2013. A Novel Separation Mechanism Device for Controlling Pico-Satellite and Separation Method. China Patent, 201 210 573 701.

Xie CX, Xu YT, Fu JZ, et al., 2014. Kinematic system design of the pico-satellite separation mechanism. *J Astronaut*, 35(6):626-632. https://doi.org/10.3873/j.issn.1000-1328.2014.06.002